

# Solar-Driven Redox Splitting of CO<sub>2</sub> Using 3D-Printed Hierarchically Channeled Ceria Structures

## Journal Article

### Author(s):

Sas Brunser, Sebastian ; Bargardi, Fabio ; Libanori, Rafael ; Kaufmann, Noëmi; Braun, Hugo; Steinfeld, Aldo ; Studart, André R.

### Publication date:

2023-10-24

### Permanent link:

<https://doi.org/10.3929/ethz-b-000626644>

### Rights / license:

[Creative Commons Attribution 4.0 International](#)

### Originally published in:

Advanced Materials Interfaces 10(30), <https://doi.org/10.1002/admi.202300452>

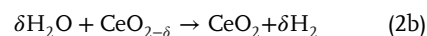
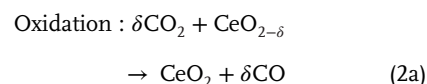
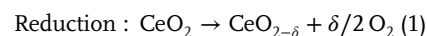
# Solar-Driven Redox Splitting of CO<sub>2</sub> Using 3D-Printed Hierarchically Channeled Ceria Structures

Sebastian Sas Brunser, Fabio L. Bargardi, Rafael Libanori, Noëmi Kaufmann, Hugo Braun, Aldo Steinfeld,\* and André R. Studart\*

Fuel produced from CO<sub>2</sub> and H<sub>2</sub>O using solar energy can contribute to making aviation more sustainable. Particularly attractive is the thermochemical production pathway via a ceria-based redox cycle, which uses the entire solar spectrum as the source of high-temperature process heat to directly produce a syngas mixture suitable for synthesizing kerosene. However, its solar-to-fuel energy efficiency is hindered by the inadequate isotropic topology of the ceria porous structure, which fails to absorb the incident concentrated solar radiation within its entire volume. This study presents the design and 3D-print of hierarchically channeled structures of pure ceria by direct ink writing (DIW) to enable volumetric radiative absorption while maintaining high effective densities required for maximizing the fuel yield. The complex interplay between radiative heat transfer and thermochemical reaction is investigated in a solar thermogravimetric analyzer with samples exposed to high-flux irradiation, mimicking realistic operation of solar reactors. Channeled structures with a stepwise optical thickness achieve a higher and more uniform temperature profile compared to that of state-of-art isotropic structures, doubling the volume-specific fuel yield for the same solar flux input. Thermomechanical stability of the ceria graded structures, DIW-printed using a novel ink formulation with optimal rheological behavior, is validated by performing 100 consecutive redox cycles.

## 1. Introduction

Renewable drop-in fuels for the transportation sector can be produced from CO<sub>2</sub> and H<sub>2</sub>O via a thermochemical redox cycle using concentrated solar energy.<sup>[1]</sup> Ceria (CeO<sub>2</sub>) has emerged as an attractive redox material because of its rapid kinetics and crystallographic stability.<sup>[2]</sup> The ceria-based redox cycle is represented by:




where  $\delta$  denotes the nonstoichiometry – a measure of the oxygen exchange capacity and, therefore, of the fuel yield per cycle. For operating conditions of the reduction at 1500 °C and 0.1 mbar and the oxidation at 900 °C and 1 bar, thermodynamics predict  $\delta = 0.04$ . The net product is a tailored syngas mixture of H<sub>2</sub> and CO which can be further

processed to liquid hydrocarbon fuels (e.g., kerosene, diesel, and gasoline) by established gas-to-liquid synthesis (e.g., Fischer-Tropsch (FT)). We have demonstrated the complete process chain to kerosene and methanol in concentrating solar dish and solar tower configurations.<sup>[3,4]</sup> This approach uses the entire solar spectrum and few process steps and can thus potentially achieve high solar energy conversion efficiencies and, in turn, economic competitiveness vis-a-vis other approaches for producing solar drop-in fuels from H<sub>2</sub>O and CO<sub>2</sub>. For example, when compared to e-fuels, the solar thermochemical pathway bypasses the solar electricity generation, the water electrolysis, and the reverse-water gas shift steps, to directly produce solar syngas of desired composition for FT synthesis, i.e., three steps are replaced by one.<sup>[3]</sup>

The cornerstone technology of the solar thermochemical fuel process is the solar reactor for performing the redox cycle. One important performance metric of the solar reactor is its solar-to-fuel energy efficiency—defined as the ratio of the calorific value of the syngas produced over the sum of the solar

S. Sas Brunser, H. Braun, A. Steinfeld  
 Department of Mechanical and Process Engineering  
 ETH Zurich  
 Zurich 8092, Switzerland  
 E-mail: aldo.steinfeld@ethz.ch

F. L. Bargardi, R. Libanori, N. Kaufmann, A. R. Studart  
 Complex Materials  
 Department of Materials  
 ETH Zurich  
 Zurich 8093, Switzerland  
 E-mail: andre.studart@mat.ethz.ch

 The ORCID identification number(s) for the author(s) of this article can be found under <https://doi.org/10.1002/admi.202300452>

© 2023 The Authors. Advanced Materials Interfaces published by Wiley-VCH GmbH. This is an open access article under the terms of the Creative Commons Attribution License, which permits use, distribution and reproduction in any medium, provided the original work is properly cited.

DOI: 10.1002/admi.202300452

energy input and any additional parasitic energy inputs. To date, maximum measured values of efficiency are still in the single digits, namely 5.6% for pure CO<sub>2</sub>-splitting and 4.1% for co-splitting CO<sub>2</sub> and H<sub>2</sub>O.<sup>[4]</sup> These results were obtained using a 50 kW solar reactor mounted on top of a solar tower and directly exposed to concentrated solar radiation delivered by a heliostat field.<sup>[4]</sup>

Essential to these previous pilot demonstrations was a simple, robust, and scalable solar reactor concept. It consisted of a cavity-receiver containing a reticulated porous ceramic (RPC) structure, made of ceria, with suitable heat and mass transfer properties as required for performing the thermochemical redox cycle at high rates. When exposed to concentrated solar radiation, its cavity shape approaches a blackbody absorber while the ceria porous structure contained inside the cavity provides the site for high-temperature heat transfer directly to the reaction through radiative penetration and volumetric absorption.<sup>[5,6]</sup> However, the homogeneous porosity of the RPC-type structure applied up to now causes Bouguer's law exponential attenuation of the incident radiation and leads to an undesired temperature gradient along the radiation path<sup>[7]</sup>. This implies that the region of the RPC structure located next to the irradiated front face is in danger of overheating, while the region far down the radiation path does not reach the desired reaction temperature and, thus, does not contribute to fuel generation. Furthermore, this unreacted region also becomes a heat sink, detrimentally affecting the efficiency. Indeed, experimental results combined with heat transfer modeling indicated that about half of the RPC inside the solar cavity-receiver is not utilized to its full potential.<sup>[4]</sup> On the other hand, deeper radiative penetration can be achieved by increasing the macroporosity of the RPC, reducing its optical thickness. This occurs at the expense of the effective density of the structure  $\rho_{\text{eff}}$ —defined as the mass of ceria per total volume—which lowers the ceria mass loading inside the solar cavity-receiver, leading to a lower volume-specific fuel yield. As a result, for maximizing the volume-specific fuel yield of a given cavity volume of the solar reactor, there is a trade-off between increasing  $\rho_{\text{eff}}$  and achieving the volumetric radiative absorption needed to ensure uniform heating of the whole volume of the porous structure to the reaction temperature. Note that using the mass-specific fuel yield as the performance metric, as commonly applied in catalytic reactors, would lead to a flawed structural design based on a thin layer of ceria on top of an inert support, which will evidently give a high value of such a mass-specific metric because of the small value of the denominator but still yield a low absolute amount of fuel produced simply because of the little mass of redox active material present. Furthermore, solar energy will be mostly wasted to heat the inert support material, which, in turn, will lead to very low values of the solar-to-fuel energy efficiency—defined as the calorific value of the fuel produced over the solar energy input. Thus, for the design of volumetric solar reactors, the volume-specific fuel yield is the applicable performance metric.

A promising solution to this trade-off is the design of hierarchically ordered structures featuring a porosity gradient along the radiation path.<sup>[8–12]</sup> When irradiated, this type of porous architectures exhibits a stepwise radiative attenuation that leads to a more uniform temperature distribution compared to that obtained with the RPC.<sup>[10]</sup> In this previous study,<sup>[10]</sup> the graded structures were manufactured by the Schwartzwald replication method, which involved 3D-printing polymer cellular lattices, im-

mersing them in a ceria slurry, and finally burning them during the ceria sintering process. However, this manufacturing methodology severely limited the amount of ceria loaded in the scaffolds and further left hollow tubular channels within the struts, resulting in mechanically unstable structures of limited  $\rho_{\text{eff}}$  (<1.8 g cm<sup>-3</sup>). This prompted us to develop an alternative fabrication technique that allows to directly 3D-print porous ceramic structures with topologies tailored to enhance volumetric radiative absorption while keeping relatively high values of  $\rho_{\text{eff}}$ .

This study presents the fabrication and testing of hierarchically ordered channeled structures, made of pure ceria, manufactured by the direct ink writing (DIW) technique using a novel ink formulation with optimal rheological behavior. The rheological properties of the ink were investigated to establish a printing process leading to channeled structures with tunable graded topology and high  $\rho_{\text{eff}}$ . These structures were characterized in terms of their temperature profiles and redox performance during the thermochemical splitting of CO<sub>2</sub>, Equations (1) and (2a), by thermogravimetric analysis (TGA) with samples directly exposed to high-flux irradiation and by carrying out multiple consecutive redox cycles. Both the manufacturing technique of porous structures with graded topologies and the experimental demonstration of their superior redox performance and stability for CO<sub>2</sub>-splitting cycles conducted under direct high-flux irradiation are essential for their successful implementation in solar reactors for efficient fuel generation.

## 2. Three-Dimensional Printing by Direct Ink Writing

The hierarchically ordered channeled structures were manufactured by the DIW technique,<sup>[13–16]</sup> where a ceria-based paste (ink) is extruded in layers at room temperature. DIW of large, crack-free structures require colloidal pastes with a high concentration of particles to minimize shrinkage<sup>[17,18]</sup> and tailored rheological properties to enable proper extrusion and bonding between printed layers while preventing shape distortion. This is possible by designing viscoelastic inks that exhibit shear-thinning response, high storage modulus, and high yield stress.<sup>[19–22]</sup> Such rheological behavior was achieved by formulating an ink with 50 vol% of electrosterically stabilized ceria particles suspended in an aqueous solution containing a rheological modifier and the gel-forming copolymer poly(ethylene oxide)-poly(propylene oxide)-poly(ethylene oxide) (PEO-PPO-PEO), which undergoes a sol-gel transition induced by temperature shifts<sup>[23]</sup> (see Section “Manufacturing of the Ceria Structures”).

The ability to reversibly switch the copolymer solutions between the sol and gel states via simple heating and cooling makes this colloidal system ideal for the formulation of extrudable inks with a high concentration of particles. Below the critical temperature of 22.5 °C, the solution is sufficiently fluid to enable the incorporation of up to 50 vol% of electrosterically stabilized ceria nanoparticles. Above this temperature, the suspension transitions to a gel state with the paste-like behavior desired for 3D printing via DIW. Based on this knowledge, we developed a protocol in which the ink constituents are added to a planetary mixer and subjected to high-speed mixing and homogenization cycles above and below the critical transition temperature, resulting in highly homogeneous pastes for printing (Figure 1).

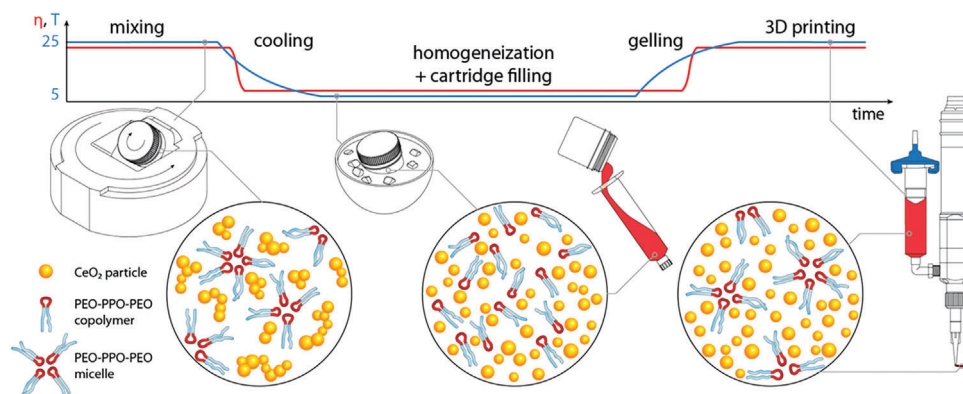


**Figure 1.** Schematics of the ink preparation workflow. The ink constituents are first mixed at room temperature ( $T$ ) in a laboratory mixer. Then, the ink is cooled in an ice bath to reduce its viscosity ( $\eta$ ) and favor the breakdown of agglomerated  $\text{CeO}_2$  particles. The resulting homogeneous ink is afterwards filled in a printing cartridge. Upon heating the cartridge back to room temperature, the poly(ethylene oxide)-poly(propylene oxide)-poly(ethylene oxide) copolymer (PEO-PPO-PEO) molecules self-assemble into micelles again, leading to a viscoelastic printable ink.

Ceria inks with such thermoresponsive formulation exhibit a clear viscoelastic response, which can be attributed to the gelation of the copolymer solution at the measuring temperature. This results in a strong shear-thinning behavior, as evidenced from the decrease in apparent viscosity by five orders of magnitude upon an increase in shear rate up to  $100 \text{ s}^{-1}$  (Figure 2a). Stress-strain measurements reveal that the ink also features an apparent yield stress of approximately 390 Pa (Figure 2b). The gel state of the ink at room temperature was confirmed by oscillatory shear experiments. Below the yield point, the ink behaves like a gel with a high storage modulus of  $10^5 \text{ Pa}$  (Figure 2c). Above the critical stress of 625 Pa, the storage modulus drops below the loss modulus, indicating the breakdown of the gel and the desired fluidization of the ink.

By quantifying the rheological properties of the ink, we were able to establish guidelines for the DIW of tunable channeled geometries. Because of the high density of ceria particles, gravity was experimentally found to cause distortion of channeled and grid-like topologies printed with nonoptimal formulations. Using simple beam theory relations (see Experimental Section), a rheological map was constructed to predict the maximum height ( $h$ ) and normalized span length ( $s$ ) that can be printed using our optimized ceria-based ink (Figure 2d). This map reveals that optimal inks can be printed into channeled objects with heights up to 15 mm and grids with filaments spanning over a length 12 times higher than their own diameter.

DIW tests confirmed the successful printing of distortion-free channeled and grid-like structures (Figure 2e,f). Experimentally, we found that the manufactured channeled structures can reach heights and span lengths significantly higher than predicted by the rheological map due to the drying of the structure during the DIW process. Indeed, rheological measurements show that partial drying of the ink during the DIW process significantly increases its storage modulus and yield stress (Figure 2c), thus increasing the maximum height and normalized span length of the printed object, respectively (Figure 2d). Inks with optimal rheological behavior were then used to 3D-print the final channeled ceria structures from stacked square grids (Figure 2g–i), utilizing printing paths, experimental setups, and characterization tools previously reported.<sup>[24]</sup> The conversion of the as-printed objects

into mechanically strong parts involved a two-step heat treatment for calcination and sintering at high temperatures. During thermal treatment, the organic additives were combusted, and pure ceria remained (see Experimental Section).

A total of eight structures of different topologies were 3D-printed. For comparisons purposes, all samples had same outer dimensions after sintering, i.e., same volume ( $2.5 \times 2.5 \times 4.0 \text{ cm}$ ). Since these structures are filling a fixed volume of the solar cavity-receiver, the performance indicators, e.g. the specific fuel yield, are normalized per unit volume of the structure. Four constant-channeled structures were printed with grids of increasing mesh densities: “Zero,” “Low,” “Medium” and “High”. Four hierarchically channeled structures were printed combining different grids. In the “Zero-Med” structure, the top half consists of a “Zero” grid and the bottom half is a “Medium” grid. In the “Low-Med” structure, the top half is the “Low” grid and the bottom half is the “Medium” grid. Finally, the “Gradient” structure combines the four aforementioned grids. In addition, two ceria RPC structures with a pore density of 10-ppi (pores per inch) were used as reference state-of-the-art samples. They were manufactured with ceria suspensions containing 30%v/v cylindrical pore formers by applying the foam replication method using centrifugal coating.<sup>[4]</sup> Every structure included four conduits of different lengths for the insertion of thermocouples (see Figure 2i). The conduits were closed at the end and served as radiation shields for the thermocouples. Three type-S thermocouples were used to measure the solid temperature at locations  $z = 2.4, 11.8,$  and  $22 \text{ mm}$  (measured from the top face  $z = 0$ ). Table 1 lists the main characteristics of each of the ten structures.

### 3. Thermochemical Performance for Redox Splitting of $\text{CO}_2$

Two experimental setups were employed to assess the thermochemical performance of the printed ceria structures: 1) the solar thermogravimetric analyzer (solar-TGA), and 2) the infrared (IR) furnace. The solar-TGA is a specially designed experimental platform for monitoring the weight change of the sample directly exposed to high-flux irradiation and undergoing a



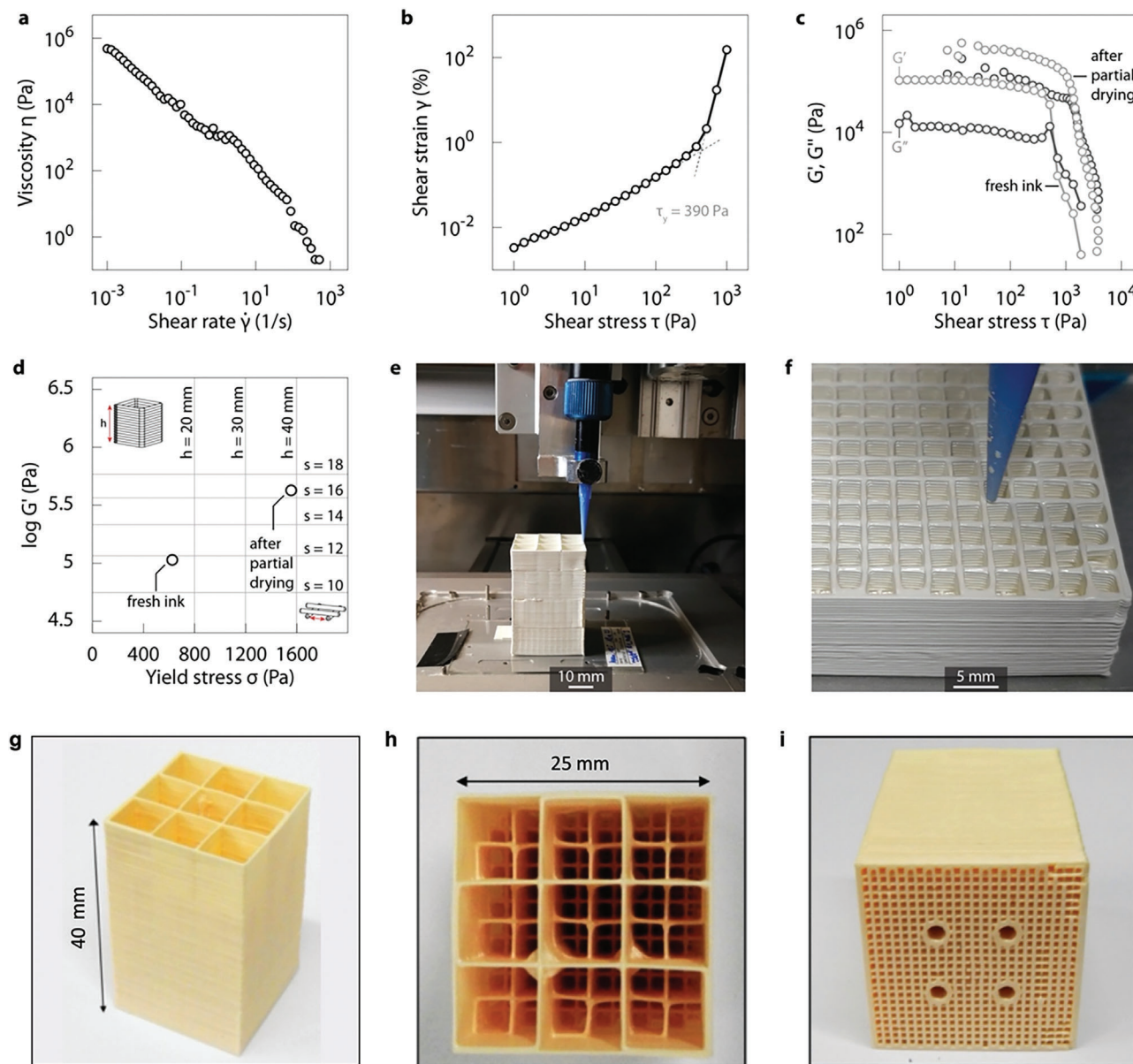


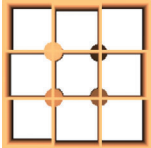
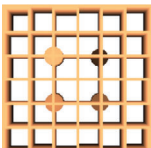
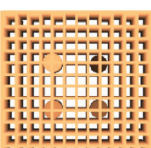
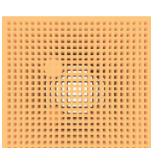
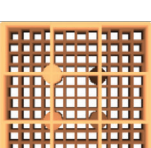
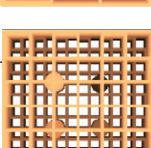
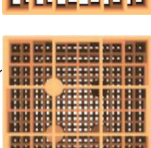
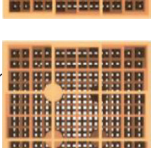
**Figure 2.** Ink rheology and 3D-printing of ceria structures. a) Apparent viscosity as a function of the applied shear rate for a fresh ceria-based ink. The ink shows the strong shear thinning behavior that favors successful paste extrusion. b) Shear measurement performed to determine the shear yield stress of the fresh ink ( $\tau_y = 390$  Pa). c) Oscillatory storage ( $G'$ ) and loss ( $G''$ ) moduli as a function of the shear stress amplitude for a freshly prepared ink and a partially dried ink. The yield stress increases with drying-induced removal of the liquid phase. d) Rheological map displaying the height ( $h$ ) and normalized spanning length ( $s$ ) achievable when printing, respectively, channeled objects and grid-like structures from a fresh ink and a partially dried ink. Horizontal and vertical lines represent data predicted from simple beam theory and from gravitational arguments, respectively (see Supporting Information). e) Photograph showing the 3D printing of a channeled object with a height up to 48 mm. f) Photograph of the ink deposition process using a nozzle with 0.41 mm inner diameter. g–i) Photographs of the structure “Gradient-1” (Table 1): g) perspective, h) top, and i) bottom views. The openings of the four conduits for the insertion of thermocouples can be seen in Figure 2i.

gas–solid thermochemical reaction. The solar-TGA was mounted at the focus of the ETH’s High-Flux Solar Simulator (HFSS) to provide a source of intense thermal radiation mimicking realistic operating conditions occurring in a solar reactor. The IR furnace was used to evaluate the mechanical and chemical stability of samples by performing multiple consecutive redox cycles with rapid radiative heating and cooling between the redox steps. Engineering details and measurement instrumentation of both

experimental setups are given in the Experimental Section (see Section Thermochemical Experimental Setups).

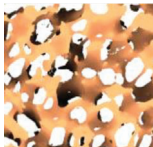
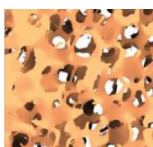
A total of 10 experimental runs were performed in the solar-TGA, one for each of the 10 investigated ceria structures (Table 1). Each run consisted of two consecutive redox cycles for  $\text{CO}_2$  splitting, Equations (1) and (2a). A representative experimental run obtained during the solar-TGA test of the sample “Medium” is shown in Figure 3. The graph displays the typical temporal

**Table 1.** Main characteristics of the 10 ceria structures: four constant-channeled structures “Zero,” “Low,” “Medium,” and “High” (samples #1-#4); four hierarchically channeled structures “Zero-Med,” “Low-Med,” “Gradient-1” and “Gradient-2” (samples #5-#8); and two reticulated porous ceramic (RPC) structures used as reference samples (samples #9-#10). All samples have same outer dimension:  $2.5 \times 2.5 \times 4.0 \text{ cm} = 25 \text{ cm}^3$ .

Structure name	Digital image (front face)align="center"	Manufacturing method	Total weight W [g]	Effective density $\rho_{\text{eff}}$ [ $\text{g cm}^{-3}$ ]	Effective porosity (layerwise)[-]
1 Zero		DIW	22.556	0.90	0.88
2 Low		DIW	36.493	1.46	0.80
3 Medium		DIW	64.630	2.59	0.64
4 High		DIW	66.171	2.65	0.63
5 Zero-Mediu		DIW	43.709	1.75	0.76 (0.88/0.64)
6 Low-Mediu		DIW	50.743	2.03	0.72 (0.80/0.64)
7 Gradier 1		DIW	47.678	1.91	0.74 (0.88/0.80/0.64/0.63)
8 Gradier 2		DIW	46.820	1.87	0.74 (0.88/0.80/0.64/0.63)

(Continued)

**Table 1.** (Continued).

Structure name	Digital image (front face)align="center"	Manufacturing method	Total weight W [g]	Effective density $\rho_{\text{eff}}$ [ $\text{g cm}^{-3}$ ]	Effective porosity (layerwise)[-]
9 RPC-A		Foam replica	28.322	1.13	0.84
10 RPC-B		Foam replica	43.818	1.75	0.76

variations of the sample's weight, temperatures across the structure, and product gas concentrations ( $\text{O}_2$  during the reduction step,  $\text{CO}$  during the oxidation step). Temperatures  $T_1$ ,  $T_2$ , and  $T_3$  were measured at depths  $Z_1 = 2.4 \text{ mm}$ ,  $Z_2 = 11.8 \text{ mm}$ , and  $Z_3 = 22 \text{ mm}$  from the illuminated surface (top). The experimental run started by preheating the sample with an incident radiative flux of 300 suns on the top face for 20 min until approximately steady-state temperatures (thermal variations  $< 2 \text{ K min}^{-1}$ ) were achieved. The reduction step was initiated by ramping up the incident radiative flux to 1000 suns under an Ar flow of  $0.5 \text{ L}_n \text{ min}^{-1}$  ( $\text{L}_n$  denotes normal liters), resulting in the steep increase of temperatures (peak at  $\approx 1500 \text{ }^\circ\text{C}$ ), which in turn drove the  $\text{O}_2$  evolution and consequently the weight drop. The radiative flux was maintained for 20 min to allow for the reduction step to be completed ( $\text{O}_2$  concentration  $< 0.005\%$ ). Next, the radiative flux was ramped down to 300 suns and maintained for 20 min until steady-state conditions were reached at the lower temperature level (peak at  $\approx 1000 \text{ }^\circ\text{C}$ ). The oxidation step started by switching the gas flow from Ar to  $0.5 \text{ L}_n \text{ min}^{-1} \text{ CO}_2$ , which drove the CO evolution and consequently the weight gain. After 20 min, the gas flow was switched back to  $0.5 \text{ L}_n \text{ min}^{-1} \text{ Ar}$ , completing the cycle. The cycle was then repeated for a second time. The second small peak of CO observed toward the end of the oxidation step ( $X_{\text{CO}} < 0.06\%$ , at times 81 and 161 min.) resulted from a small amount of CO accumulated in the reaction zone while switching from  $\text{CO}_2$  to Ar, and finally swept out by the Ar flow. During this switching, it took a few seconds to re-establish the sweeping Ar flow rate because of the response time of the flow controller, as confirmed by the mass flow readings and the total pressure monitoring. The total masses of  $\text{O}_2$  and CO released during the reduction and oxidation steps,  $m_{\text{O}_2}$  and  $m_{\text{CO}}$ , were derived from the samples' weight drop and gain, respectively. They correspond to a mean  $\delta = 0.004$ . The molar ratio  $n_{\text{CO}}/n_{\text{O}_2} = 1.9 \pm 0.25$  (error within the range of the measurement accuracy) indicates total selectivity for the splitting reaction  $\text{CO}_2 = \text{CO} + \frac{1}{2}\text{O}_2$  in two separate streams of CO and  $\text{O}_2$ . There was no evidence of carbon deposition or any other side reaction. Results for all structures are listed in Table S1 (Supporting Information).

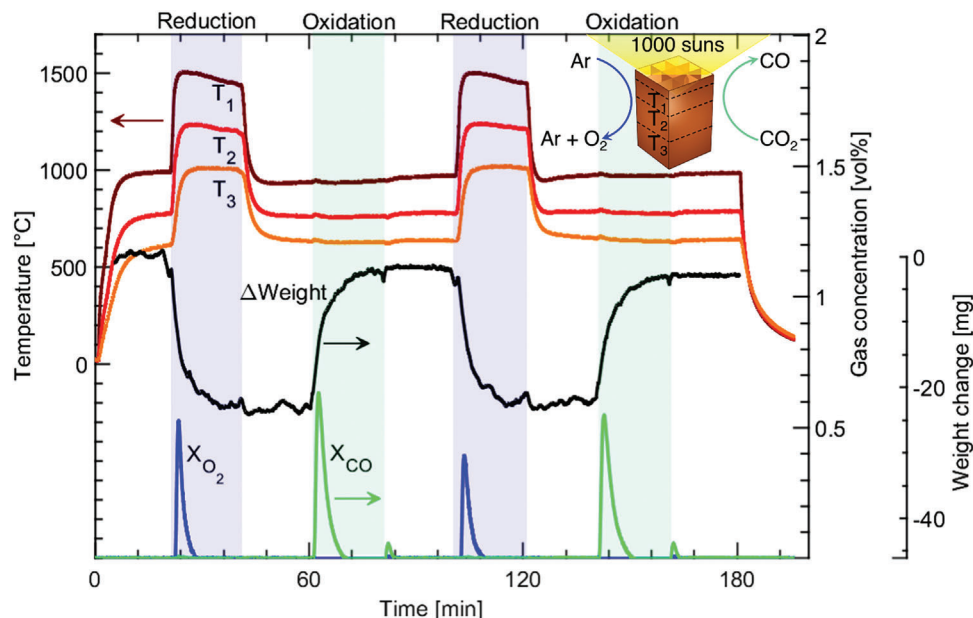


**Figure 3.** Representative temporal variations of the weight, temperatures across the structure, and product gas concentrations ( $O_2$  during the reduction step,  $CO$  during the oxidation step) of an experimental run with two consecutive redox cycles of the sample “Medium.” The experimental conditions are: reduction with  $0.5 L_n \text{ min}^{-1}$  Ar and 1000 suns; oxidation with  $0.5 L_n \text{ min}^{-1}$   $CO_2$  and 300 suns.

Steady-state temperature profiles measured across the sample during the reduction step are shown in **Figure 4a** ( $z = 0$  is the top face exposed to the incoming radiative flux). Clearly, the channeled architecture strongly affects the radiative heat transfer and the resulting temperatures. The nongraded channeled structures “Medium” and “High” as well as the RPC structures displayed monotonically decreasing temperature profiles, with the highest values at the top (front) in the range 1250–1450 °C and lowest values at the bottom (rear) in the range 820–1010 °C. The temperature gradient for the RPC was significant and reached a mean

value of  $23 \text{ }^\circ\text{C mm}^{-1}$ . These results are consistent with the predicted exponential attenuation of incoming radiation for structures with homogeneous porosity. Note that the higher temperatures at the front translate into higher emissive radiative losses to the surroundings, reducing the overall absorbed radiation and thus the overall temperature level at equilibrium. It is evident that making these structures longer ( $>4 \text{ cm}$ ) would be detrimental because the reaction temperatures would not be reached in the added material and solar energy would be wasted to heat this unreactive added material, thereby reducing the volume-specific

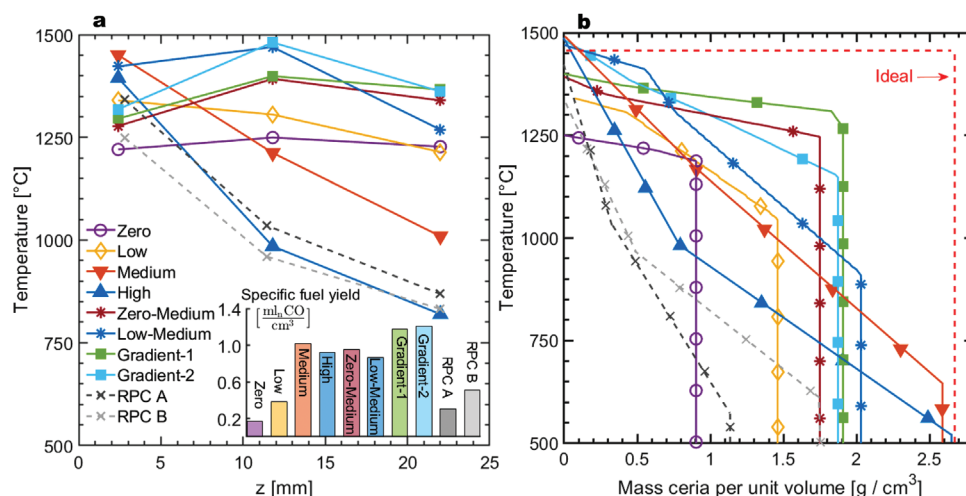


**Figure 4.** a) Steady-state temperature profiles across the sample during the reduction step for the 10 structures of Table 1. In this graph,  $z = 0$  corresponds to the top (front) face exposed to the incoming high-flux radiation. Insert: volume-specific fuel yield ( $\text{mL}_n \text{ CO}$  generated per unit volume) during the oxidation step of the  $CO_2$ -splitting cycle. b) Normalized mass of ceria per unit volume ( $x$ -axis) above a given temperature ( $y$ -axis) at the end of the reduction step for the 10 structures of Table 1. The experimental conditions are: reduction with  $0.5 L_n \text{ min}^{-1}$  Ar and 1000 suns.



yield of solar fuel. As expected, the much higher porosity of the nongraded channeled structures “Zero” and “Low” (Table 1) enabled deeper penetration of incident radiation due to their low optical thickness. This resulted in a more uniform temperature distribution along the samples’ depth, although at a much lower overall temperature level. The low  $\rho_{\text{eff}}$  of these structures (Table 1) is an intrinsic disadvantage because of the relatively low specific loading of ceria per unit volume of the solar reactor. On the other hand, higher  $\rho_{\text{eff}}$  often adversely affects the optical thickness and the potential for volumetric absorption, resulting in a more pronounced temperature gradient. Consequently, regions of the ceria structure down the radiation path do not reach the reduction temperature and thus become heat sinks without contribution to fuel generation. This is the case for the homogeneous-porosity structures “RPC-A,” “RPC-B,” “Medium,” and “High”. In contrast, the gradient-porosity structures exhibited higher and more uniform temperature values despite their higher values of  $\rho_{\text{eff}}$  (1.9 g cm<sup>-3</sup>) compared to those for the RPCs (1.13–1.75 g cm<sup>-3</sup> Table 1). Furthermore, they achieved their peak temperatures deeper within the volume due to the volumetric effect, effectively reducing re-radiation heat losses through the front (exposed) walls and leading to higher overall temperatures.<sup>[9]</sup> The best performing structures across all ten designs are the “Gradient-1” and “Gradient-2,” which reached a peak  $T = 1400$  °C and 1481 °C and a mean gradient lower than 11 and 18 °C mm<sup>-1</sup>, respectively.

To further illustrate the ability of the hierarchically channeled architecture in increasing the fraction of active redox material, we evaluated the amount of ceria that reached the reduction temperature for the different investigated structures exposed to high-flux irradiation. Figure 4b shows the normalized mass of ceria per unit volume ( $x$ -axis) that is heated above a temperature level ( $y$ -axis) at the end of the reduction step, assuming linear interpolation of the measured temperatures and constant temperature at equal heights. For an ideal structure, all of its mass would be heated to the reduction temperature (in the range 1300–1500 °C, depending on the O<sub>2</sub> partial pressure), thus showing an ideal flat line (indicated by the dashed red line) above 1300 °C. However, both RPCs show a steep decreasing line, indicating that only a small fraction of the structure (<15%) is heated above 1250 °C, while the rest of the structure’s temperature rapidly decreases. In contrast, the “Gradient-1” and “Gradient-2” structures have most of their total mass (90% and 50%, respectively) heated above 1300 °C. These results reveal that the hierarchically channeled architecture is an effective design to enhance the volumetric absorption by stepwise increasing the optical thickness along the radiation path while maintaining a relatively high  $\rho_{\text{eff}}$ . Such features significantly increase the loading of the redox material in the solar reactor that can reach the reaction temperatures.

The specific fuel yield, i.e., the amount of CO generated per unit volume of the structure, is shown in the insert of Figure 4a. The results are consistent with the thermodynamics of nonstoichiometric ceria,<sup>[25]</sup> which predicts that higher temperatures should lead to higher O<sub>2</sub> release during the reduction step (Equation 1) and, in turn, to higher fuel generation (H<sub>2</sub>/CO) during the oxidation step (Equation 2a,b). The results also corroborate the trade-off between increasing  $\rho_{\text{eff}}$  and achieving volumetric radiative absorption as higher  $\rho_{\text{eff}}$  do not necessarily

translate to higher volume-specific fuel yield. For example, the “High” structure, which has the highest  $\rho_{\text{eff}}$  (Table 1), gives a lower specific fuel yield than that of the “Medium,” “Zero-Medium,” “Gradient-1” and “Gradient-2” structures, because of the relatively stronger radiative attenuation of the isotropic (non-graded) structures. Remarkably, “Gradient-1” and “Gradient-2” produced approximately three times more CO than the RPC-A, having only 67% more mass. In comparison to RPC-B, they produced 2.3 times more CO with only 8% more mass. Thus, as expected from the temperature profiles of Figure 4b, the experimental results indicate that the printed hierarchically channeled design can more than double the specific fuel yield compared to the state-of-the-art RPCs applied in current solar reactors.

Note that all the experimental runs of the solar-TGA were performed under exactly the same boundary conditions of solar radiative power input, i.e., 1000 suns irradiation over 6.25 cm<sup>2</sup> top face ( $P_{\text{solar}} = 0.625$  kW) during the endothermic reduction step. It is therefore reasonable to anticipate that, if the RPC-type structure inside the solar cavity-receiver is replaced by the Gradient-type structure, the fuel yield will be approximately doubled for the same solar energy input, i.e., the solar-to-fuel energy efficiency will be approximately doubled and reach values exceeding 10% for the 50 kW solar reactor, even without heat recovery.<sup>[4]</sup>

Preliminary thermomechanical testing in the IR furnace with consecutive cycles revealed that several samples lost mechanical integrity at locations where imperfections (e.g., cracks) were present from the manufacturing process. Vacuum coating<sup>[26]</sup> was then performed to successfully infiltrate these cracks with ceria slurry (details in the Experimental Section), forming an additional ceria layer of 149±15 μm thickness, as determined by computer tomography and scanning electron microscopy (SEM). Long-term stability was validated for the vacuum-coated DIW structures in 100 consecutive redox cycles.

## 4. Conclusions

We have developed a novel ink formulation with optimal rheological behavior for DIW of tunable graded structures made of pure ceria. These porous structures are applied in the design of solar reactors for the thermochemical splitting of CO<sub>2</sub> with concentrated solar radiation. In particular, hierarchically ordered channels with stepwise optical thickness circumvented the exponential radiative attenuation of isotropic topologies and achieved a higher and more uniform temperature profile compared to that of the state-of-the-art reticulated structures. This in turn led to a twofold higher specific fuel yield per unit volume for the same solar radiative flux input. Tailoring the structure’s porosity by tuning the graded topology was found to be an effective design strategy to increase the effective density (i.e., the redox active material loading in the solar reactor) without compromising the volumetric radiative absorption needed to ensure that the entire volume of the porous structure contributes to fuel generation. Such an approach can significantly boost the solar-to-fuel energy efficiency of the solar reactor and, thereby, the economic viability of solar fuels production.



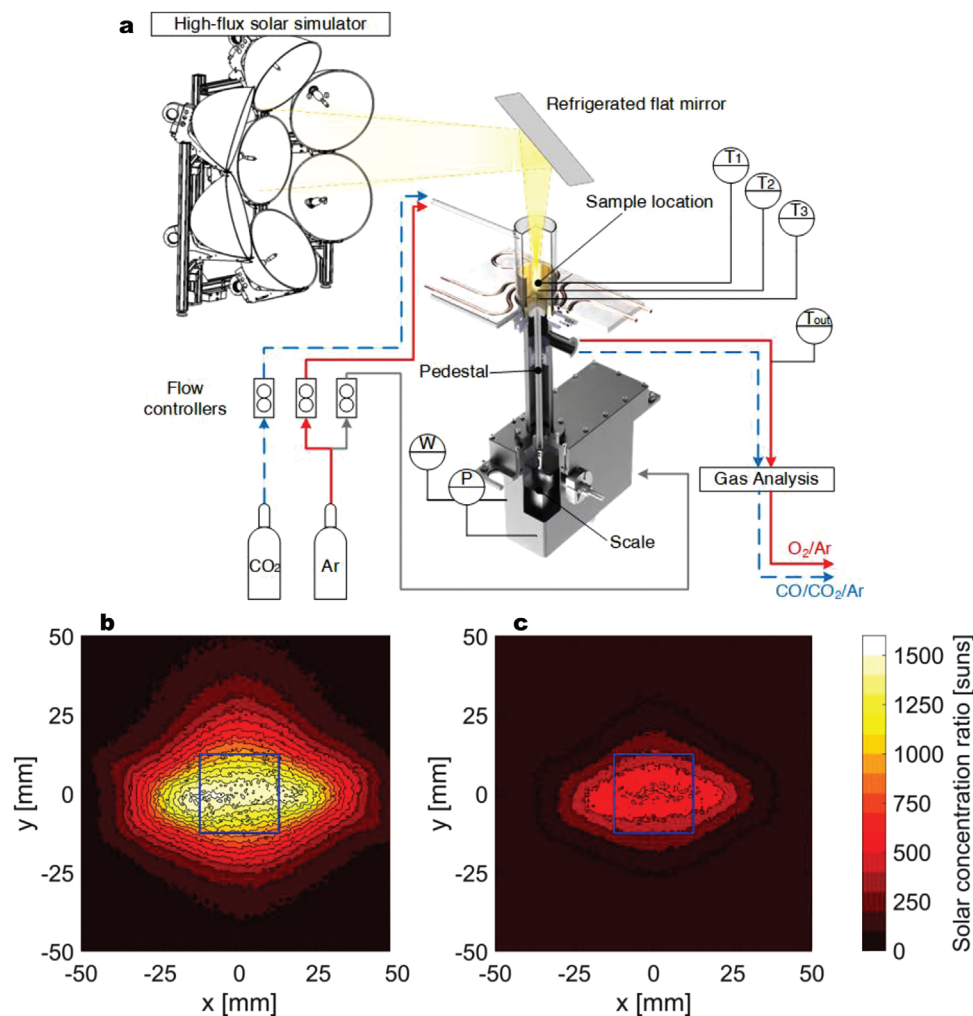


**Figure 5.** a) Scheme of the experimental setup depicting the high-flux solar simulator (HFSS), the solar thermogravimeter analyzer (solar-TGA), the 45°-mirror, the gaseous reactants and products gas handling, and the control and measurement instrumentation. Legend: W: weight scale; P: pressure sensor; T: thermocouple. Dimensions are not to scale. The measured radiative flux maps of the HFSS applied in the experimental runs are shown in (b) and (c). On average, b) 1000 suns, and c) 300 suns are incident on the sample's top square face, indicated by the blue square, during the reduction and the oxidation, respectively.

## 5. Experimental Section

**Manufacturing of the Ceria Structures:** The DIW technique was applied to manufacture the ceria porous samples with hierarchically ordered channels (samples 1–8 in Table 1). Water-based colloidal suspensions with ceria particle concentrations up to 50 vol% were prepared through an electrosteric stabilization mechanism using a polyacrylic acid salt. The ceria particles display a monomodal size distribution with an average size of 1  $\mu\text{m}$  (Figure S1a, Supporting Information). At pHs higher than 3, the polyelectrolyte becomes negatively charged and adsorbs on the surface of the ceria particles to form an electrosteric layer that prevents particle agglomeration. Zeta potential measurements confirmed the adsorption of polyacrylate on the colloid surface and the formation of negatively charged ceria particles at pH values above 3 (Figure S1b, Supporting Information).

A PEO-PPO-PEO copolymer (Pluronic F-127, Sigma-Aldrich) was used to prepare ceria pastes with satisfactory rheological properties for DIW. An attractive feature of aqueous solutions of this copolymer is that it undergoes a sol–gel transition that can be induced by temperature shifts (Figure S1c, Supporting Information).<sup>[23]</sup> For this particular copolymer, gels are formed upon heating of the solution beyond the sol–gel transition temper-

ature (critical micelle temperature), above which the macromolecules self-assemble into a phase separated percolating network. Such sol–gel transition temperature depends on the concentration of copolymer in solution, which can be tuned to enable the formation of a gel close to room temperature. Oscillatory rheology shows that such a temperature-triggered sol–gel transition increases the storage modulus of PEO-PPO-PEO aqueous solutions by five to six orders of magnitude (Figure S1d, Supporting Information).

Besides the storage modulus, rheological measurements were also performed to assess the yield stress of PEO-PPO-PEO aqueous solutions in the gelled state. The results indicate that aqueous solutions containing 20 wt% of copolymer exhibit a well-defined yield stress of 60–100 Pa at 25 °C (Figure S1e,f, Supporting Information). Since this value falls within the lower limit of the yield stress level usually required to print distortion-free structures (>100 Pa), this work also explored other approaches to further increase the yield stress of the copolymer solutions. The substitution of 10 wt% of the PEO-PPO-PEO aqueous solution with limonene oil was found to be an effective means to increase the yield stress and the storage modulus by a factor of 3 and 2, respectively, of the copolymer gel (Figure S1e,f, Supporting Information). Given the very low solubility of the oil in water,

such an effect probably arises from the formation of limonene droplets within the gel, which enhance the interconnectivity and strengthen the copolymer network. The influence of limonene on the printing behavior of the ink is discussed elsewhere.<sup>[24]</sup>

Printing of ceria structures was possible by tuning the rheological properties of the pastes (Figure 2). To establish guidelines for the DIW of channeled and grid-like geometries, this work considered simple beam theory and gravitational arguments. This allowed us to map out the set of storage modulus ( $G'$ ) and yield stress ( $\sigma_y$ ) levels required to print distortion-free structures (Figure 2d). For channeled architectures, the height of the printed object is the limiting factor, since it determines the weight carried by the bottom printed layer. To prevent gravity-induced distortion of the bottom layer, the height of the printed object should be lower than the critical value  $h = \sigma_y / \rho g$ , where  $\sigma_y$  is the yield stress of the ink,  $\rho$  is the density of the ink, and  $g$  is the gravitational acceleration. For grid-like structures, the span length ( $L$ ) of a filament hanging in air between two underlying print lines is an important geometrical parameter to create open architectures. Earlier work has shown that the span length ( $L$ ) normalized by the filament diameter ( $D$ ) depends on the storage modulus of the ink ( $G'$ ) as follows:  $s = L/D = [G'/(1.4wD)]^{1/4}$ , where  $w$  is the specific weight of the ink ( $\rho g/4$ ).<sup>[20]</sup> In the estimation, a typical filament diameter of 400  $\mu\text{m}$  and a suspension density of 4.07  $\text{g cm}^{-3}$  (50 vol% particles) were assumed.

Drying of the paste during printing enables printing of taller channeled structures and grids with larger filament spacings (Figure 2). Complete drying of the structure is eventually achieved by leaving the printed object at room temperature for 24 h. The experiments show that the as-printed structures undergo linear shrinkage of less than 1% (<0.5 mm) after complete drying. This increases the volume fraction of ceria particles in the system from 50 vol% in the initial ink to 52.5 vol% in the fully dried structure.

After drying, the conversion of the printed objects into mechanically strong parts involves a two-step heat treatment for calcination and sintering of the structure at high temperatures. During calcination, the organic phase of the structure is removed through the thermal decomposition of the copolymer and remaining oil. To ensure complete removal of the organic phase without damaging the object, it is essential to heat up the material to the decomposition temperature of the organic phase and provide enough time for the resulting gases to diffuse out of the structure. By performing TGA of dried as-printed inks, a calcination protocol was established for the effective thermal decomposition of the organic phase. The TGA results indicate significant mass losses at temperatures between 170 °C and 260 °C, which correspond to the thermal decomposition of the copolymer (Figure S2a, Supporting Information). By holding the material for a minimum of 2 h above this critical temperature range, crack-free structures were obtained after the calcination process (Figure S2b, Supporting Information). Upon removal of the organic phase, the material does not show any considerable linear shrinkage.

Calcination was followed by a standard sintering procedure, in which the material is heated to 1600 °C and maintained at this temperature for 5 h to promote densification of the calcined structure (Figure S2b, Supporting Information). Scanning electron microscopy of sintered samples showed that these conditions allowed for the development of a dense ceria microstructure with limited grain growth (Figure S2c, Supporting Information). The average grain size of the sintered ceria was found to be 5  $\mu\text{m}$ , which is on the same order of magnitude of values previously reported for ceria-based reactors.<sup>[27]</sup> Archimedes measurements reveal a remaining strut porosity of 7% which results in a relative density of 93%. To enable densification up to this relative density level, the material undergoes linear and volumetric shrinkages of approximately 17% and 44% during the sintering process. From these experimental shrinkage values, the volume fraction of solids in the printed material was estimated to be 49 vol% before sintering, which is in agreement with the fraction of ceria particles in the ink formulation (50 vol%).

The established calcination and sintering protocols allowed us to manufacture tall channeled monoliths featuring high-aspect-ratio dense walls (Figure S2d,e, Supporting Information). The thickness of the walls is ultimately defined by the diameter of the printing nozzle, the print path and the shrinkage associated to the drying, calcination, and sintering steps.

Using a nozzle diameter of 400  $\mu\text{m}$  and the optimized ink formulation, it is possible to reach wall thickness down to 290  $\mu\text{m}$  in 5 cm-tall monolithic pieces. Since this wall thickness lies in a length scale at which the ceria is expected to undergo reduction in less than 10 s at 1500 °C,<sup>[28,29]</sup> the monolith design ensures that all the oxide present in the structure contributes to the redox reaction. The programming of the print path via computer-aided design enabled the 3D print ceria monoliths with deliberately tuned line densities along the height of the structure (Figure S2e, Supporting Information). Monoliths with fill factors of 0.590 (D4), 0.338 (D3), 0.202 (D2), and 0.124 (D1) and line densities of 0.833 (D4), 0.417 (D3), 0.208 (D2), and 0.104  $\text{mm}^{-1}$  (D1) were produced either with a graded or with uniform designs (Figure S2e,f, Supporting Information).

For the mechanical stability of the printed samples, a vacuum infiltration and coating process was performed following a reported protocol<sup>[26,30]</sup> using a ceria slurry<sup>[10]</sup> where 30% of the ceria weight is added in the form of nanopowder. The vacuum infiltration allowed to fill completely and partially some of the manufacturing induced cracks in the printed samples.

**Thermochemical Experimental Setups:** The experimental setup for the measurements with the solar thermogravimeter analyzer (solar-TGA) is shown schematically in Figure 5. It is a unique experimental platform for monitoring the weight change of the sample directly exposed to high-flux radiation in a controlled atmosphere.<sup>[31]</sup> The sample holder (Alumina Alsint 99.7) is enclosed by a sealed transparent quartz dome ( $\varnothing 70 \times 2.5 \times 160$  mm, Quartz HSQ 300) and rests in a vertical pedestal ( $\varnothing 26 \times 3 \times 39$  mm rod, Alumina Alsint 99.7) which transfers the weight to the scale at the bottom. The measured weight is corrected for buoyancy effects as a function of the temperature, pressure, and gas composition. Three wireless platinum-shielded Type-S thermocouples measure the structure's temperature at three separate locations. Argon (99.995% purity) and  $\text{CO}_2$  (99.995% purity) are injected by four mass flow controllers (EL-Flow Select, Bronkhorst). A gas analyzer (Ultramat 23, Siemens) measures the outlet gas composition. The solar-TGA was mounted at the focus of ETH's High-Flux Solar Simulator (HFSS): an array of Xe arcs, each closed-coupled with a truncated ellipsoidal specular reflector, provides a source of intense thermal radiation that mimics the radiative heat transfer characteristics of highly concentrating solar systems. A 45° refrigerated flat mirror re-directs the radiative beam from the HFSS downwards toward the top of the sample. The radiative flux incident on the top square face of the sample was measured optically by a calibrated CCD camera focused on a Lambertian target and validated with a water-cooled calorimeter placed at the exact location. The radiative flux measurements, shown in Figure 5b, were taken at the two radiative power levels of the HFSS applied in the experimental runs. The values displayed in the flux map correspond to the solar concentration ratio (in units of "suns") given by the measured radiative flux intensity normalized by 1  $\text{kW m}^{-2}$  (equivalent to 1 sun).

The measurements of the solar-TGA runs for all 10 structures are displayed in Table S1 (Supporting Information). Listed are total  $\text{O}_2$  and  $\text{CO}$  released during the reduction and oxidation steps of two consecutive  $\text{CO}_2$ -splitting cycles, respectively, and the molar ratio between them based on the weight change of cycle no. 2. The on-line measurement of  $\text{O}_2$  concentration could only be used qualitatively due to its limited accuracy below 0.6 vol%, while the integration of the on-line measurement of  $\text{CO}$  concentration matched  $m_{\text{CO}}$  within 7%. Within the range of the measurement accuracy,  $n_{\text{CO}}/n_{\text{O}_2} = 2$  in all experimental runs, except for samples "Zero" and "RPC A" which were not re-oxidized to the initial nonstoichiometry  $\delta$  during cycle no. 2. There was no evidence of carbon deposition or any other side reaction, indicating total selectivity for  $\text{CO}_2$  splitting into two separate streams of  $\text{CO}$  and  $\text{O}_2$ .

The experimental setup for the measurements with the IR furnace is shown schematically in Figure S3 (Supporting Information). It was used for the stability studies of samples subjected to multiple consecutive redox cycling. The IR furnace (VHT-E48, Ulvac Riko) delivers intense thermal radiation from high-temperature heating elements toward a horizontal quartz tube containing the sample, mimicking the heat transfer characteristics of directly irradiated solar reactors. Since the furnace's internal walls are gold-coated and refrigerated, the samples can be rapidly heated and cooled between the redox steps. Consecutive redox cycles are carried

out by applying temperature swings between set furnace temperatures of 1500 °C and 800 °C while simultaneously altering the feed gas composition between Ar and CO<sub>2</sub> for the reduction and oxidation steps, respectively. The duration of the reduction (8.5 min.) and oxidation (18.5 min.) steps are fixed for all cycles. The gas flow rate is controlled by three electronic mass flow controllers (EL-Flow select, Bronkhorst). The exiting gas composition is determined by a on-line gas analyzer (Ultramat 23, Siemens). An S-type thermocouple measures the sample temperature. The sample's dimensions were 25 × 25 × 12 mm to fit inside the quartz tube.

Figure S4 (Supporting Information) shows the measured total volumes of O<sub>2</sub> (blue squares) and CO (green circles) released during the reduction and oxidation steps, respectively, for 105 consecutive CO<sub>2</sub>-splitting redox cycles with the structure "High" that was vacuum coated. The gas output decreased by 18.8% over the first 100 cycles. This apparent degradation is attributed to the incomplete sample re-oxidation for the given fixed duration of the oxidation step (18.5 min., same for each cycle), as confirmed by re-oxidizing the sample to its initial state at 800 °C in air for 2 h (cycle #101), after which the released volumes went back up to the initial levels (cycles #102 to #105). Incomplete oxidation was also manifested by the coloration of the tested sample before cycling, after cycle #100, and after cycle #101, as shown by the photographs of Figure S5 (Supporting Information). Before cycling, the sample exhibited color chamois, typical of pure cerium(IV) oxide.<sup>[32]</sup> After cycle #100, the sample was grey, indicating nonstoichiometric ceria (CeO<sub>2-δ</sub>).<sup>[33]</sup> After cycle #101, the sample turned back to its original color before cycling, indicating complete oxidation.

The incomplete re-oxidation is the result of the reaction rate slowing down as the cycling progresses. Figure S6 (Supporting Information) shows the CO concentration (blue-yellow lines) for representative cycles #2, #20, #40, #60, #80, and #100, sample's measured temperature (red, dashed) for cycles #2 and #100, and set furnace temperature (red, solid) for all cycles, as a function of time during the oxidation step of the 100 consecutive CO<sub>2</sub>-splitting redox cycles of Figure S4 (Supporting Information). The variation of the sample's measured temperature was identical for all cycles, confirming that the cycle-to-cycle operational conditions did not vary. However, the reaction rate clearly slowed down from cycle to cycle, as evidenced by the decreasing peak and slope of the curves. Since the duration of the oxidation step is fixed to 18.5 min. for each cycle, the oxidation was prematurely interrupted before it reached completion, which explains the decreasing trend of Figure S4 (Supporting Information). This effect is due presumably to a degradation in the microporosity of the coated layer, although there was no visible degradation using SEM of sections representative of the whole sample. Figure S7 (Supporting Information) shows the SEM pictures before (a) and after 100 consecutive cycles (b). Interestingly, the red arrow in (a) indicates the location of infiltration of ceria slurry into a void which resulted from a manufacturing defect of the 3D-printed sample (nonbonded filaments), applied by the vacuum coating technique.

## Supporting Information

Supporting Information is available from the Wiley Online Library or from the author.

## Acknowledgements

S.S.B. and F.L.B. contributed equally to this work. This work was funded in part by the Swiss Federal Office of Energy (Grant No. SI/502552-01). The authors thank P. Haueter and J. Urech for technical support with the solar-TGA and IR-furnace setups, and S. Kistler and S. Schreiber for technical support with the manufacturing of the ceria structures. The Data Availability Statement has been updated on 24 October 2023, after initial online publication of the Version of Record.

## Conflict of Interest

The authors declare no conflict of interest.

## Author Contributions

A.S. conceived the project idea. A.S. and A.R.S. managed and supervised the project. S.S.B., F.B., R.L., A.S., and A.R.S. contributed to the design of the channeled ceria structures. F.L.B. prepared the printing G-code and optimized the printing paths. F.L.B. and N.K. developed and characterized the inks for the DIW technique and 3D-printed the ceria structures. F.L.B. designed and optimized the experimental printing setup. F.L.B., R.L. and A.R.S. discussed and interpreted the results from the ink development and printing at all stages. S.S.B. performed the vacuum infiltration coating. S.S.B. and A.S. designed the experimental redox setups. S.S.B. and H.B. executed and analyzed the redox experiments. S.S.B. and F.L.B. prepared the figures. A.S. and A.R.S. wrote the manuscript with input from all authors.

## Data Availability Statement

The data that support the findings of this study are available from the corresponding authors upon reasonable request.

## Keywords

3D printing, ceramics processing, solar fuels, solar reactors, thermochemical fuel

Received: June 1, 2023  
Published online: August 11, 2023

- [1] M. Romero, A. Steinfeld, *Energy Environ. Sci.* **2012**, *5*, 9234.
- [2] W. C. Chueh, C. Falter, M. Abbott, D. Scipio, P. Furler, S. M. Haile, A. Steinfeld, *Science* **2010**, *330*, 1797.
- [3] R. Schappi, D. Rutz, F. Dahler, A. Muroyama, P. Haueter, J. Lilliestam, A. Patt, P. Furler, A. Steinfeld, *Nature* **2022**, *601*, 63.
- [4] S. Zoller, E. Koepf, D. Nizamian, M. Stephan, A. Patané, P. Haueter, M. Romero, J. Gonzalez-Aguilar, D. Liefstink, E. de Wit, S. Brendelberger, A. Sizmann, A. Steinfeld, *Joule* **2022**, *6*, 1606.
- [5] C. C. Agrafiotis, I. Mavroidis, A. G. Konstandopoulos, B. Hoffschmidt, P. Stobbe, M. Romero, V. Fernandez-Quero, *Sol. Energy Mater. Sol. Cells* **2007**, *91*, 474.
- [6] A. L. Ávila-Marín, *Sol. Energy* **2011**, *85*, 891.
- [7] S. Ackermann, M. Takacs, J. Scheffe, A. Steinfeld, *Int. J. Heat Mass Transfer* **2017**, *107*, 439.
- [8] F. Gomez-Garcia, J. Gonzalez-Aguilar, S. Tamayo-Pacheco, G. Olalde, M. Romero, *Sol. Energy* **2015**, *121*, 94.
- [9] S. Luque, G. Menéndez, M. Roccabruna, J. González-Aguilar, L. Crema, M. Romero, *Sol. Energy* **2018**, *174*, 342.
- [10] M. Hoes, S. Ackermann, D. Theiler, P. Furler, A. Steinfeld, *Energy Technol.* **2019**, *7*, 1900484.
- [11] A. L. Avila-Marín, J. Fernandez-Reche, S. Gianella, L. Ferrari, presented at SOLARPACES 2018: International Conference on Concentrating Solar Power and Chemical Energy Systems, Casablanca, Morocco, October **2019**.
- [12] M. Pelanconi, M. Barbato, S. Zavattoni, G. L. Vignoles, A. Ortona, *Mater. Des.* **2019**, *163*, 107539.
- [13] X. Zhang, Y. Zhang, Y. Lu, S. Zhang, J. Yang, *J. Eur. Ceram. Soc.* **2020**, *40*, 4366.
- [14] B. A. E. Ben-Arfa, S. Abanades, I. M. M. Salvado, J. M. F. Ferreira, R. C. Pullar, *Nanoscale* **2022**, *14*, 4994.
- [15] C. Minas, D. Carnelli, E. Tervoort, A. R. Studart, *Adv. Mater.* **2016**, *28*, 9993.
- [16] J. A. Lewis, J. E. Smay, J. Stuecker, J. Cesarano, *J. Am. Ceram. Soc.* **2006**, *89*, 3599.

- [17] X. G. Xia, G. L. Duan, *Mater. Res. Express* **2021**, *8*, 015403.
- [18] F. L. Bargardi, H. Le Ferrand, R. Libanori, A. R. Studart, *Nat. Commun.* **2016**, *7*, 13912.
- [19] A. L. Troksa, H. V. Eshelman, S. Chandrasekaran, N. Rodriguez, S. Ruelas, E. B. Duoss, J. P. Kelly, M. R. Ceron, P. G. Campbell, *Mater. Des.* **2021**, *198*, 109337.
- [20] J. E. Smay, J. Cesarano, J. A. Lewis, *Langmuir* **2002**, *18*, 5429.
- [21] J. A. Lewis, *Adv. Funct. Mater.* **2006**, *16*, 2193.
- [22] D. Kokkinis, M. Schaffner, A. R. Studart, *Nat. Commun.* **2015**, *6*, 8643.
- [23] E. Gioffredi, M. Boffito, S. Calzone, S. M. Giannitelli, A. Rainer, M. Trombetta, P. Mozetic, V. Chiono, *Procedia CIRP* **2016**, *49*, 125.
- [24] F. L. Bargardi, *Architected Inorganic Materials for Energy Conversion and Storage Doctoral Thesis*, ETH Zürich, Zurich, Switzerland **2022**.
- [25] R. J. Panlener, R. N. Blumenthal, J. E. Garnier, *J. Phys. Chem. Solids* **1975**, *36*, 1213.
- [26] U. F. Vogt, M. Gorbar, P. Dimopoulos-Eggenschwiler, A. Broenstrup, G. Wagner, P. Colombo, *J. Eur. Ceram. Soc.* **2010**, *30*, 3005.
- [27] P. Furler, J. Scheffe, D. Marxer, M. Gorbar, A. Bonk, U. Vogt, A. Steinfeld, *Phys. Chem. Chem. Phys.* **2014**, *16*, 10503.
- [28] R. C. Pullar, R. M. Novais, A. P. F. Caetano, M. A. Barreiros, S. Abanades, F. A. C. Oliveira, *Front. Chem.* **2019**, *7*, 601.
- [29] S. Ackermann, J. R. Scheffe, A. Steinfeld, *J. Phys. Chem. C* **2014**, *118*, 5216.
- [30] S. Maleksaeedi, H. Eng, F. E. Wiria, T. M. H. Ha, Z. He, *J. Mater. Process. Technol.* **2014**, *214*, 1301.
- [31] M. Takacs, S. Ackermann, A. Bonk, M. Neises-von Puttkamer, P. Haueter, J. R. Scheffe, U. F. Vogt, A. Steinfeld, *AIChE J.* **2017**, *63*, 1263.
- [32] A. C. Neish, *J. Am. Chem. Soc.* **1909**, *31*, 517.
- [33] S. Ackermann, A. Steinfeld, *Sol. Energy Mater. Sol. Cells* **2017**, *159*, 167.